Article:
Xu, N., Wang, D., Taylor, C.M. et al. (2026) Adhesive layer formation and its dual role in tribological performance and surface integrity of Ti-6Al-4V: implications for the machining process. Tribology International, 214, Part B. JTRI_111228. ISSN: 0301-679X

https://doi.org/10.1016/j.triboint.2025.111228

Tribology International 214 (2026) 111228

Contents lists available at ScienceDirect

Tribology International

journal homepage: www.elsevier.com/locate/triboint

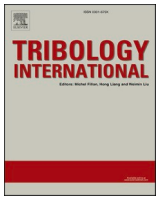

Adhesive layer formation and its dual role in tribological performance and surface integrity of Ti-6Al-4V: Implications for the machining process

Nan Xu [a,*], Dongze Wang [a,*], Chris Taylor [b], Jack Secker [b], Greg de Boer [a], Harvey Thompson [a], Nikil Kapur [a], Ardian Morina [a,*]

[a] Institute of Functional Surfaces, School of Mechanical Engineering, University of Leeds, Leeds LS2 9JT, United Kingdom
[b] AMRC, University of Sheffield, Advanced Manufacturing Park, Wallis Way, Catcliffe, South Yorkshire S60 5TZ, United Kingdom

ARTICLE INFO

Keywords:
Titanium alloy
Machining
Adhesive layer
Numerical modelling
Minimum quantity lubrication (MQL)

ABSTRACT

The poor machinability of Ti-6Al-4V (Ti64), characterized by adhesive and abrasive wear, low thermal conductivity, and high chemical reactivity, continues to hinder efficient manufacturing. Among these challenges, adhesive layer formation on tool flank faces remains poorly understood despite its critical influence on tool degradation and workpiece surface integrity. To address this, this study investigates the tribological behavior of WC/Co-Ti64 pin-on-disc sliding contacts under dry and minimum quantity lubrication (MQL) conditions through both experimental and numerical approaches. Experimental results show that thick, stable, and intact adhesive layers transferred from Ti64 discs was formed on WC/Co pin surfaces under dry and low MQL flowrate conditions. These layers are associated with reduced friction coefficients and lower disc wear but simultaneously contribute to compromised surface integrity. Comparative boundary element method (BEM) simulations with 316 L stainless steel reveal that the lower elastic modulus of Ti64 adhesive layers significantly reduces nominal contact pressure and subsurface von Mises stress, lowering friction coefficients and enhancing mechanical stability of adhesive layer. However, the accompanying increase in surface roughness intensifies local stress concentrations and result in thicker work-hardened layers on Ti64 disc, which align well with BEM simulation results. Conversely, high MQL flowrate inhibited adhesive layer formation, leading to higher friction and wear but producing smoother surfaces and thinner work-hardened layer. The findings offer new mechanistic insights into complex interplay between adhesive layer, lubrication and surface topography, and present the first direct evidence of the dual role of adhesive layer: reducing friction and tool-side wear but compromising workpiece surface integrity.

1. Introduction

Titanium alloys, particularly Ti64, are increasingly employed in aerospace, biomedical, automotive, and general industrial applications due to their excellent strength-to-weight ratio, corrosion resistance, heat resistance, and biocompatibility [1,2]. These properties make Ti64 a preferred material for critical component such as aircraft structural parts, medical implants, engine components, and other high-performance industrial tools. The global Ti64 titanium alloy market was valued at USD 3.2 billion in 2024 and is projected to reach USD 5.5 billion by 2033, representing a compound annual growth rate (CAGR) of 7.3 % from 2026 to 2033, driven primarily by its expanding use in advanced manufacturing and high-performance industries [3]. Despite these advantageous properties, Ti64 presents significant machining challenges, classifying itself as a difficult-to-machine material. These challenges primarily stem from its high chemical reactivity, low thermal conductivity, low elastic modulus, and strong tendency for work-hardening [4,5]. At elevated cutting temperatures, Ti64 shows strong chemical affinity with tool materials, leading to severe adhesive and diffusion wear [5,6]. These interactions frequently result in the formation of adhesive layers at the tool/workpiece interface, which, upon detachment, can cause localized tool damage or failure [7]. Moreover, the inherently low thermal conductivity of Ti64 causes significant heat accumulation in the cutting zone, exacerbating tool wear and degradation [8]. Its low elastic modulus further contributes to elastic recovery, dimensional inaccuracies, and potential machining instability due to chatter [9]. Collectively, these factors accelerate tool deterioration, necessitate frequent tool replacements, and substantially

* Corresponding authors.
E-mail addresses: N.Xu@leeds.ac.uk (N. Xu), mn17d2w@leeds.ac.uk (D. Wang), A.Morina@leeds.ac.uk (A. Morina).

https://doi.org/10.1016/j.triboint.2025.111228
Received 1 July 2025; Received in revised form 10 September 2025; Accepted 22 September 2025
Available online 23 September 2025

increase manufacturing costs [10]. Thus, there is an urgent need to deepen the understanding of underlying wear mechanisms and their interplay with the material properties of Ti64 to optimize machining processes and enhance tool life and surface integrity.

Among the various wear modes encountered during machining operations, flank wear is particularly critical as it directly influences tool life and the final surface integrity of machined components [11]. Flank wear progression is governed by mechanical and thermal loads acting at the cutting tool, determined by interactions involving contact stress, temperature distributions, and material properties [12]. These interactions significantly influence the machined surface integrity, a crucial factor in determining the functionality and durability of high-performance components [13]. Key surface integrity characteristics, including surface topography, plastic deformation, near-surface work hardening, residual stress, and potential phase transformations, are heavily dependent on tool wear dynamics [14]. Achieving and maintaining desirable surface integrity is especially challenging for titanium alloys, given that their distinctive properties can readily induce accelerated tool flank wear [15].

Previous studies have explored various aspects of tool wear and surface integrity in titanium machining. Liang and Liu demonstrated that increased flank wear under dry cutting conditions leads to greater plastic deformation and diminishes compressive residual stress on machined surfaces [16]. Lin et al. developed numerical models to study tool-workpiece interactions influenced by flank wear [17], while Karpat and Özel investigated thermal effects during the machining process, showing that wider flank wear land widths elevate cutting temperatures and degrade surface quality [18]. Furthermore, Toubhans et al. identified that the formation of built-up edge (BUE) and built-up layers contributes to force instability during machining [19]. BUE was reported to degrade surface quality, alter tool geometry, and shorten tool life through material adhesion and tribochemical reactions [15,20,21]. However, a stable BUE can mitigate micro-milling tool wear and improve surface roughness under specific conditions [22,23], promoting strategies being developed to exploit BUE formation for optimizing surface finish and extending tool service life [15,23,24].

Although these studies provide valuable insights into specific wear mechanisms involved in titanium machining, such as adhesive, BUE effects and diffusion wear [25,26], the detailed formation process and mechanical behaviour of those adhesive layers on the tool flank face remain inadequately explored [27]. In particular, the role of these adhesive layers in governing tool degradation and surface integrity across varying machining conditions is poorly characterized [25]. This knowledge gap restricts the optimization of machining parameters and tool designs, limiting efforts to effectively mitigate wear and enhance tool life during titanium alloy machining [26].

To fill in this gap, the present study integrates experimental testing with numerical modelling to investigate adhesive layer formation and its effects under controlled sliding conditions:

- Complex machining dynamics were reduced to fundamental tribological tests using a custom-designed high-speed, high-load pin-on-disc tribometer to approximate the tool flank face/workpiece contact while boundary-element-method-based simulations provided complementary analysis of adhesive layer from the perspective of contact mechanics.
- By synergistically combining experimental and numerical methods, the effects of mechanical properties, normal load, sliding speed, and MQL flow rate on adhesive layer formation were systematically studied. The dual role of adhesive layers in reducing friction and wear while potentially degrading workpiece surface integrity were found and elucidated.

These findings offer valuable mechanistic insights into the complex interaction between adhesive layer formation, lubrication and surface topography in governing the tribological behavior and subsurface integrity. It helps establish a foundation for optimizing machining strategies, tool design, and lubrication protocols for Ti64, stainless steel 316 L and other difficult-to-machine materials. Built on this work, our next-step research aims to prevent the formation of Ti alloy adhesive layers and enhance surface integrity in actual machining operations through optimized lubrication and cooling strategies.

Table 1
Lubricating oil properties.

Oil type	Viscosity cst at 40 °C	Flash point (°C)	Pour point (°C)
Polyol ester	24	260	−59

Table 2
Mechanical properties of pin and disc materials.

Materials	*E* (GPa)	*ν*	*H* (GPa)	*YS* (GPa)	*C* (W/m·k)
WC/Co (Pin)	600	0.21	14	4.7	100
Ti6Al4V (Disc)	113	0.34	3.2	1.07	7
316 L (Disc)	193	0.25	2.2	0.73	16

Note: *E*, elastic modulus; *ν*, Poisson's ratio; *H*, hardness; *YS*, yield strength is 1/3 of the hardness; *C*, thermal conductivity. Yield stress of materials (assumed to be H/3) in the current study [28,29].

2. Methodology

2.1. Tribological experiments

Tribological tests were performed using a bespoke high-speed, high-load pin-on-disc tribometer. The friction forces (F_f) were measured using a load cell and the friction coefficients (f_c) were calculated using the equation $f_c = F_f / F_n$, where F_n is the applied normal load. The disc samples, made of Ti64 and 316 L stainless steel, were 40 mm in diameter. A fixed upper pin made of tungsten carbide with 10 wt% cobalt (WC/Co) and with a 10 mm diameter hemispherical head served as the counterpart. Tests were conducted under ambient conditions with sliding speeds ranging from 47 to 141 m/min, contact pressures between 1.2 and 2.5 GPa (simulating effect of different cutting depths), and a fixed duration of 30 s (approximating a single cutting process). Here, 316 L was selected as a comparison material for its relevance in engineering applications and its contrasting mechanical properties with Ti64, allowing for a clearer interpretation of the material-dependent tribological responses. A new set of samples was used for each test. Lubrication was provided using an ester-based neat oil (ROCOL, UK) delivered at variable flowrate (0–44 ml/h) through a minimum quantity lubrication (MQL) system (Allube Ltd, UK). The key properties of the lubricant are summarized in Table 1. Table 2 lists the relevant physical properties of the pin and disc materials. To measure the contact temperature during sliding, a thermocouple channel was machined into each pin using Electrical Discharge Machining (EDM). A K-type thermocouple was inserted at the top of the channel with the junction located approximately 1 mm away from the tribological contact surface of the pin.

2.2. Materials characterization

The morphology and composition of adhesive layers formed on the pin surfaces were analysed using Scanning Electron Microscopy (SEM, Carl Zeiss EVO MA15) equipped with an Energy Dispersive X-ray Spectrometer (EDX, Oxford Instruments AZtecEnergy system). To examine the subsurface microstructure in the frictional contact regions, cross-sectional specimens were prepared using a focused ion beam (FIB, FEI Helios G4 CX DualBeam FIB-SEM) and subsequently characterized via SEM and EDX. A 3D non-contact optical profilometer (NPFLEX,

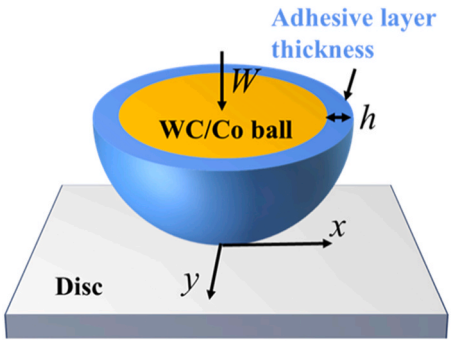

Fig. 1. Schematic illustration of the elastic layered contact model used in BEM simulations. The WC/Co pin used in the experiment is simplified as a rigid sphere which is coated with a uniform adhesive layer and pressed against a Ti64 or 316 L disc under a normal load W in this model. The model assumes perfect bonding between the adhesive layer and the pin, and dry contact between the layered pin and disc.

Bruker) was used to characterize the topography and wear tracks on both pin and disc surfaces. Surface mechanical properties, including hardness and elastic modulus of the disc samples, were evaluated using a nano-indenter (Micro Materials, UK).

2.3. *Numerical Modelling: Boundary Element Method (BEM) simulation*

Boundary Element Method (BEM) simulations were conducted to complement the experimental investigations and reveal the underlying mechanisms associated with adhesive layer formation during sliding. In the model, the WC/Co pin was simplified as a rigid sphere with a perfectly bonded elastic transfer layer representing the adhesive film, while the Ti64 or 316 L disc was treated as a homogeneous elastic half-space (Fig. 1). Dry contact conditions were assumed, neglecting lubrication and thermal effects. To determine the contact tractions and subsurface stresses, different from the conventional half-space contact problems, for which explicit analytical solutions are mathematically tractable in the spatial domain such as the Boussinesq integral [30] and Cerruti's solutions [31], the layered contact problem needs to be solved by deducing the response functions in the frequency domain first and then using the reverse Fourier transform to obtain the corresponding solutions in the spatial domain, as practiced in the work of Wang et al. [32]. Computational techniques, including the discrete convolution fast Fourier transform (DC-FFT) [33] and conjugate gradient method (CGM) [34] were applied to accelerate the computational speed of the algorithm. Model validation was performed against published results for elastic layered contact problems by Wang et al. [35]. Simulations investigated the effects of adhesive layer thickness and surface roughness on contact pressure distribution and subsurface von Mises stress evolution. A concise description of the numerical formulation, grid refinement strategies, and algorithmic implementation for solving elastic layered contact problems, along with relevant validation studies, is provided in the Supplementary material.

3. Results and discussion

Fig. 2a illustrates the experimental setup for the pin-on-disc tribological tests, in which both friction force and contact temperature were recorded simultaneously. Figs. 2b and 2c present the average friction coefficient and maximum temperature under varying test conditions (Hertzian contact pressures: 1.2–2.5 GPa; sliding speeds: 47–141 m/min) for two kinds of disc materials: Ti64 and 316 L stainless steel. The

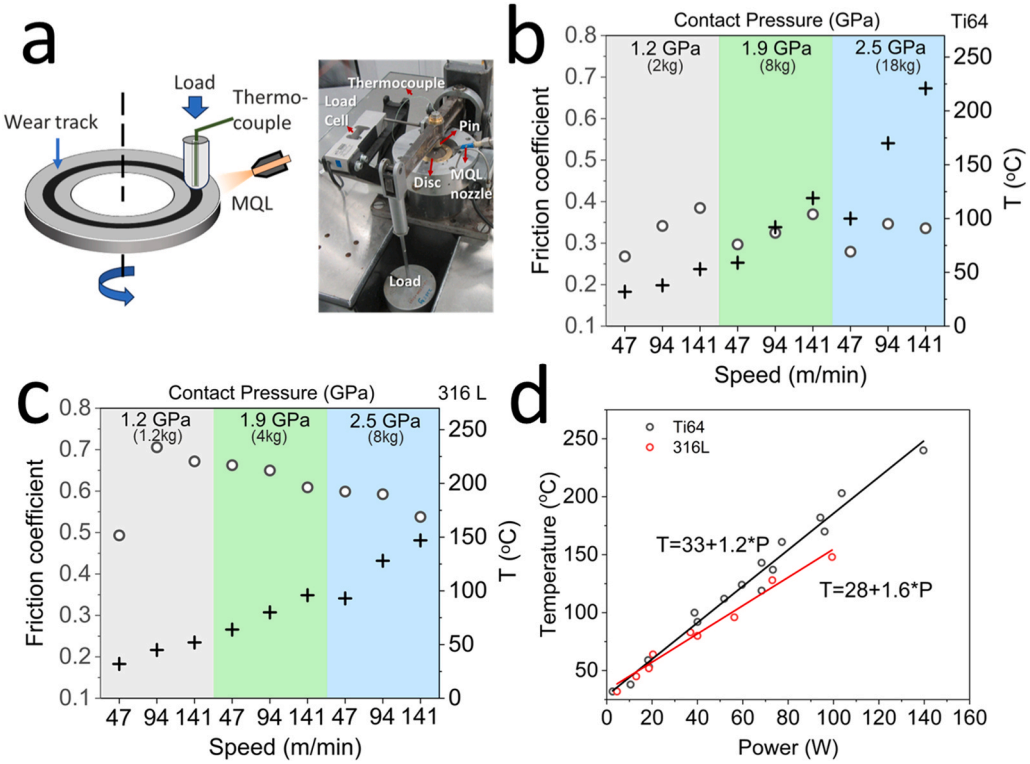

Fig. 2. (a) Schematic of the tribological test setup, showing the arrangement for simultaneous measurement of friction force and contact temperature using a thermocouple embedded in the pin. (b) Dry sliding test results for WC/Co pin against Ti64 disc under applied loads of 2, 8, and 18 kg, corresponding to maximum Hertzian contact pressures of 1.2, 1.9, and 2.5 GPa, respectively. (c) Dry sliding test results for WC/Co pin against 316 L stainless steel disc under applied loads of 1.2, 4, and 8 kg, yielding similar maximum contact pressures of 1.2, 1.9, and 2.5 GPa, respectively. Test duration for all cases was 30 s. (d) Correlation between friction-induced heating power and the resulting temperature measured by the thermocouple for both Ti64 and 316 L disc conditions. Note: in Fig. 2(b) and (c), the data points marked with circles and plus signs correspond to average friction coefficient (left side of y axis) and maximum temperature (right side of y axis), respectively.

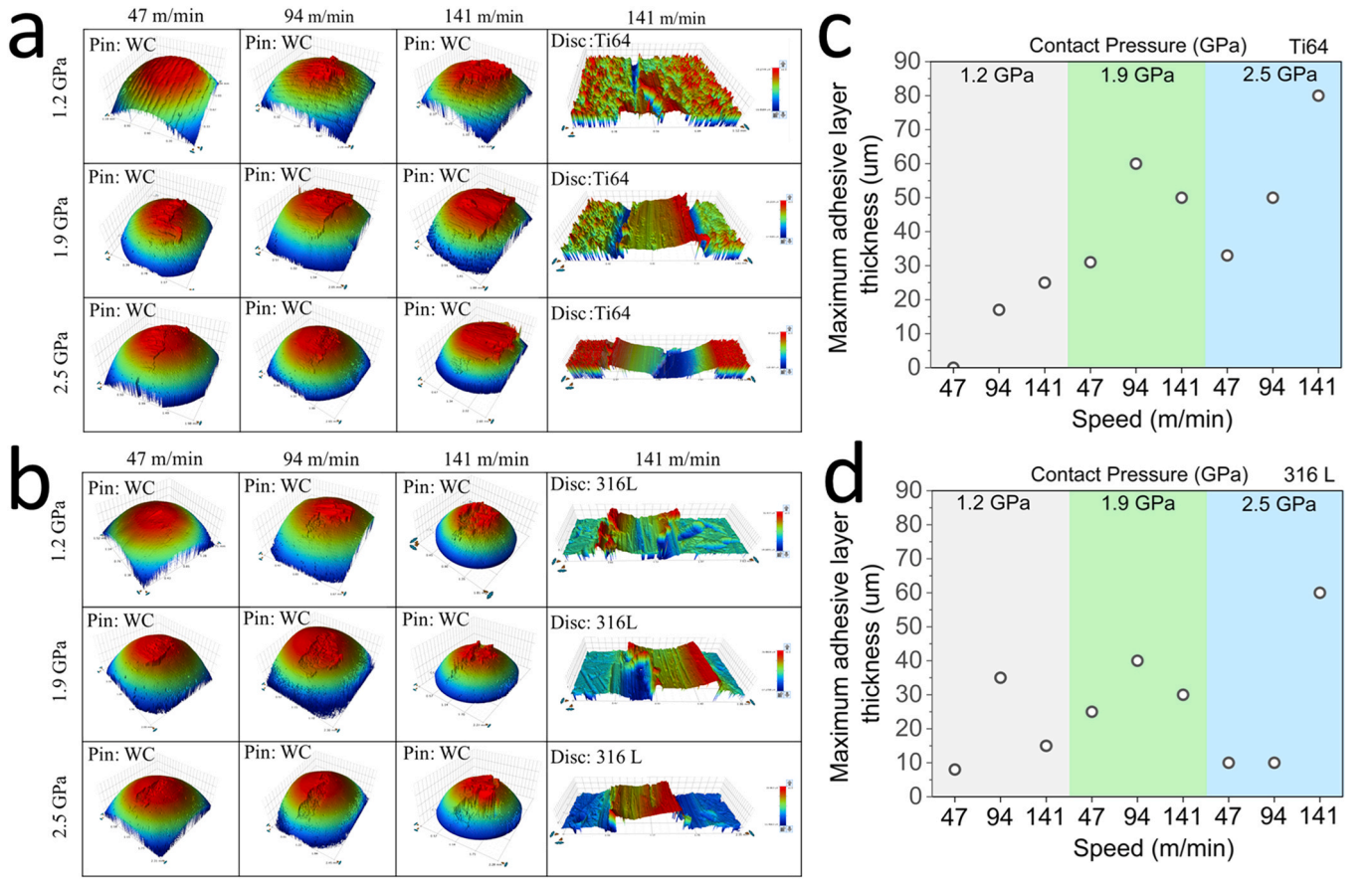

Fig. 3. Images showing the surface morphologies of wear scars on the pins and discs (a, WC/Co pins and Ti64 discs; b, WC/Co pins and 316 L stainless steel discs) and the maximum thicknesses of the adhesive layers formed on the pin surfaces (c, WC/Co pins and Ti64 discs; d, WC/Co pins and 316 L discs) under different test conditions. Test time: 30 sec.

WC/Co-Ti64 contact system exhibited a relatively stable average friction coefficient of approximately 0.32 ± 0.04 across all conditions. In contrast, the WC/Co-316L system showed consistently higher friction values, averaging 0.61 ± 0.07. The temperature profiles in Figs. 2b and 2c reveal similar trends for both disc materials, with temperature increasing with the sliding speed and load. However, the rate of temperature increase is obviously greater when Ti64 is used as the disc material. This can be attributed to differences in thermal conductivity between the two materials: Ti64 has a low thermal conductivity of approximately 7 W/m·K, compared to 16 W/m·K for 316 L stainless steel. According to the relation $Q = F{\cdot}V$, where Q is the heat flow, F is the friction force, and V is the sliding velocity, energy dissipation at the contact interface is governed by both mechanical and thermal factors [36]. Fig. 2d shows a linear correlation between heating power and measured surface temperature for both Ti64 and 316 L discs. Notably, under equivalent power input, the surface temperature of Ti64 is significantly higher than that of 316 L, further confirming the impact of lower thermal conductivity on temperature accumulation during sliding.

As displayed in Figs. 3a and 3b, the wear surfaces of tribo-tested pins and discs were characterized using 3D optical profilometry. Distinct differences in adhesive layer formation were observed depending on the counterpart disc material. When paired with Ti64 discs, intact and continuous adhesive layers with well-defined structures were formed on the pin contact surfaces. The maximum thickness of these layers exhibited a positive correlation with both sliding speed and applied load, reaching approximately 80 μm under the most severe testing conditions (highest load and speed). In contrast, tests conducted with 316 L discs resulted in discontinuous adhesive layers with irregular thicknesses that varied significantly across different test parameters, suggesting inherent instability in layer formation. Comparative analysis revealed that adhesive layers formed with Ti64 discs were consistently thicker than those formed with 316 L discs, particularly under high-load and high-speed conditions (Figs. 3c and 3d). Composition analysis through SEM/EDX in Fig. 4 confirmed that the adhesive layers were primarily composed of materials transferred from the respective disc counterparts. The Ti-rich layers originating from Ti64 discs maintained structural integrity, while the Fe-rich layers derived from 316 L discs exhibited fragmented morphologies. The transfer of material from the disc to the pin surface significantly influenced wear behavior. The formation of an adhesive layer on the pin altered the contact conditions, leading to uneven material removal from the disc surface. This process resulted in increased surface roughness and the development of irregular wear tracks, as illustrated in Figs. 3a and 3b. Such deterioration in surface quality can adversely affect the performance and longevity of components in practical applications.

Considering the morphological variations of the adhesive layer formed on the pin surface when interfaced with different disc materials, and its subsequent impact on surface quality, a detailed stress analysis was conducted for the layered pin-on-disc contact through the numerical modelling based on the boundary element method, as presented in Fig. 5. The contact was simplified as a ball-on-disc configuration, where the adhesive layer was modelled as an outer shell on the ball surface (Fig. 1). The stability of the adhesive layer was evaluated using the normalized von Mises stress, defined as the ratio of von Mises stress (σ_{vm}) to yield strength (σ_{yield}) of the adhesive material. A higher $\sigma_{vm}/\sigma_{yield}$ ratio indicates an increased risk of adhesive layer instability and potential material removal under sliding contact conditions. This criterion aligns

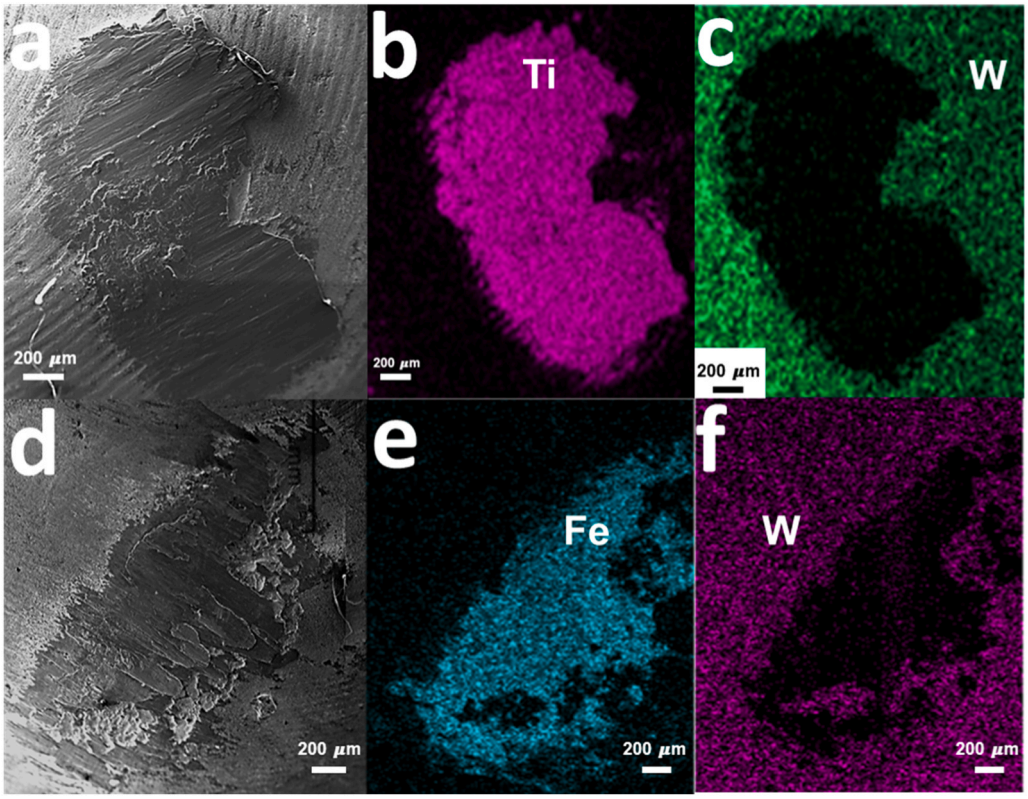

Fig. 4. SEM and EDX mapping images showing the morphologies and composition of adhesive layers for two test conditions (a-c, sample materials of WC/Co pin and Ti64 disc, speed of 94 m/min, load of 2.5 GPa, test time of 30 sec; d-f, sample materials of WC/Co pin and 316 L stainless steel disc, speed of 94 m/min, load of 2.5 GPa), test time of 30 sec.

with the wear simulation approaches of Akchurin et al. [37] and Li et al. [38], where potential wear particles were identified when the nodal von Mises stress exceeds the material yield stress. Notably, the actual set of wear particles were determined when additional conditions are satisfied, details of which can be found in the work of Li et al. [38]. Fig. 5a presents the cross-sectional normalized von Mises stress distributions for Ti64 adhesive layers with varying thicknesses (0.1–100 μm) under a normal load of 8 kg. It is observed that the regions of maximum normalized stress initially appear beneath the surface of the adhesive layer and shift progressively toward the ball/adhesive layer interface as the layer thickness increases. A similar trend is observed for the 316 L adhesive layers in Fig. 5c. Figs. 5b and 5d present the evolution of maximum $\sigma_{vm}/\sigma_{yield}$ ratio with increasing adhesive layer thickness for Ti64 and 316 L, respectively, distinguishing the locations of stress maxima on the surface, interface, and within the bulk. Quantitatively, the maximum $\sigma_{vm}/\sigma_{yield}$ ratio for Ti64 ranges from approximately 1.3–2.25, while the ratio for 316 L varies from 2.1 to 2.9. This comparison indicates that Ti64 adhesive layers exhibit greater mechanical stability under the same loading conditions, as higher $\sigma_{vm}/\sigma_{yield}$ ratio in the 316 L case suggests a higher probability of yielding and layer instability. These findings are consistent with earlier surface characterization results (Figs. 3 and 4), which showed a more continuous and intact adhesive layer in the Ti64 condition.

To further verify the impact of adhesive layer on the tribological performance, friction tests were conducted using Ti64 discs and WC/Co pins under both dry and lubricated conditions. An ester-based lubricating oil was applied via Minimum Quantity Lubrication (MQL) Systems at varying flowrates ranging from 0 (dry) to 44 ml/h. As shown in the Fig. 6a, the friction coefficient displayed the lowest value under dry conditions and low MQL flowrate of 4 ml/h. In contrast, higher MQL flowrates resulted in increased friction coefficients. The corresponding wear area values on the discs under different lubricated conditions are displayed in the Fig. 6b. Notably, the wear area values under high flowrate significantly increased by four times compared to dry condition and low flowrate of 4 ml/h. This trend contrasts with intuitive expectations, where lubrication is generally assumed to reduce friction and wear.

To elucidate the observed tribological behavior, surface morphology analysis of the pin and disc wear tracks was performed using a 3D optical profilometer (Fig. 6c). Under dry and low flowrate (4 ml/h) conditions, obvious adhesive layers were observed on the pin surfaces. In contrast, under higher MQL flow rates (12–44 ml/h), the adhesive layer was either minimal or absent, and no measurable wear was detected on the pin. This suggests that increased oil supply effectively prevented the formation of adhesive layers, consistent with previous finding that adequate lubrication can prevent third-body layer formation during sliding of Ti64 alloys [39]. A quantitative summary in Fig. 6d illustrates the relationships between oil flowrates and key tribological parameters, including disc surface roughness, disc wear volume, average friction coefficient, and maximum adhesive layer thickness. Notably, conditions promoting adhesive layer formation (dry and low MQL flowrate) consistently corresponded to lower friction coefficients and reduced disc wear. Conversely, higher MQL flow rates, which inhibited adhesive layer formation, were associated with increased friction and wear. These results suggest that the presence of adhesive layer, typically associated with material transfer, plays a key role in reducing both friction and disc wear in WC/Co-Ti64 contacts.

To clarify the influence of adhesive layers on contact mechanics and tribological performance, BEM-based modelling was employed to simulate the contact pressure [32]. In this model, the adhesive layer formed on the pin surface was represented as an outer shell on a spherical ball with a diameter of 10 mm, corresponding to the round head of the WC/Co pin, as shown in Fig. 1.

Figs. 7a and 7b present the simulation results for Ti64 and 316 L

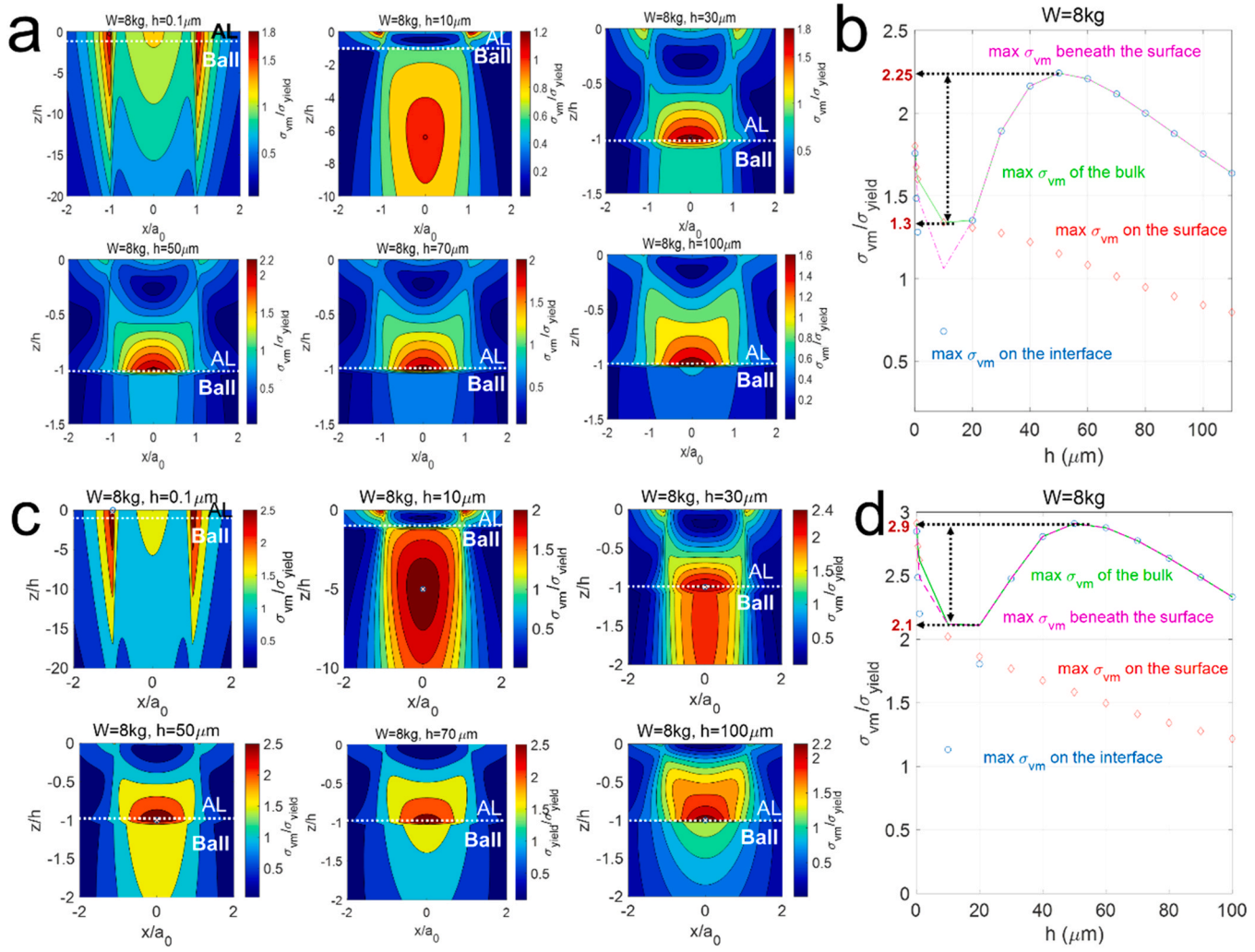

Fig. 5. Cross-sectional von Mises stress distribution analysis at the interface between the adhesive layer (AL) and the ball using a BEM-based contact model. (a) Distribution of von Mises stress for different AL thicknesses when Ti64 is used as the adhesive layer material (applied load: 8 kg). (b) Variation of maximum normalized Von Mises stress ($\sigma_{vm}/\sigma_{yield}$) with adhesive layer thickness corresponding to (a). (c) Von Mises stress distribution for different AL thicknesses when 316 L stainless steel is used as the adhesive layer material (applied load: 8 kg). (d) Variation of maximum normalized von Mises stress ($\sigma_{vm}/\sigma_{yield}$) with adhesive layer thickness corresponding to (c). Note: σ_{vm} is the von Mises stress; σ_{yield} is the yield stress of the corresponding adhesive layer material; z/h represents the normalized vertical coordinate within the contact region, where h is the layer thickness.

discs, respectively, under an applied load of 8 kg and varying adhesive layer thicknesses (0.1–100 μm). In the absence of an adhesive layer (h = 0 μm), the maximum contact pressures predicted by the Hertzian model were approximately 1.9 GPa for Ti64 and 2.4 GPa for 316 L, attributed to the lower elastic modulus of Ti64. As the adhesive layer thickness increased from 0.1 to 100 μm, a notable decrease in contact pressure and a corresponding increase in contact radius were observed. For Ti64, the maximum contact pressure decreased from 1.9 to 1.56 GPa, accompanied by an increase in contact radius from 142 to 160 μm. In contrast, the contact pressure for 316 L reduced from 2.4 to 2.0 GPa, with the contact radius expanding from 124 to 140 μm. These results suggested that materials with a lower elastic modulus tend to generate a larger real contact area, which leads to a reduction in nominal contact pressure. This change in contact mechanics directly impacts the tribological performance. As shown in Fig. 6, tests with Ti64 discs under dry and low MQL conditions, where stable adhesive layers were present, consistently exhibited lower friction coefficients and reduced disc wear. The suppression of adhesive layer formation at higher MQL flow rates led to increased contact pressure, correlating with higher friction and wear. Moreover, the compositional differences between disc materials also affect tribological behavior, with Ti64 consistently exhibiting lower friction coefficients compared to 316 L (Fig. 2,). These findings underscore the dominant influence of adhesive layer morphology and composition on the contact interface, highlighting their critical role in determining overall tribological behavior.

To further examine the surface integrity (e.g., subsurface microstructure and mechanical property) of the Ti64 disc following tribological testing, cross-sectional analysis and nano-indentation measurements were conducted. Fig. 8a shows the focused ion beam (FIB)-milled cross-section of the wear scar on the Ti64 disc. Under dry sliding conditions (Fig. 8b), a pronounced work-hardening layer of approximately 14 μm thick was observed beneath the worn surface. In contrast, under MQL conditions with high oil flowrate of 44 ml/h, the plastically deformed zone was significantly thinner, measuring approximately 2 μm (Fig. 8c). The corresponding load-displacement curves from nano-indentation tests (Fig. 8d) further illustrate this trend. The unworn surface exhibited a hardness of 3.1 GPa and an elastic modulus of 118 GPa. After dry sliding, these values increased markedly to 6.3 GPa and 135 GPa, respectively, consistent with substantial work hardening. Under high MQL flowrate condition, the hardness and elastic modulus values were intermediate (4.4 GPa and 128 GPa), reflecting a less degree of surface work-hardening.

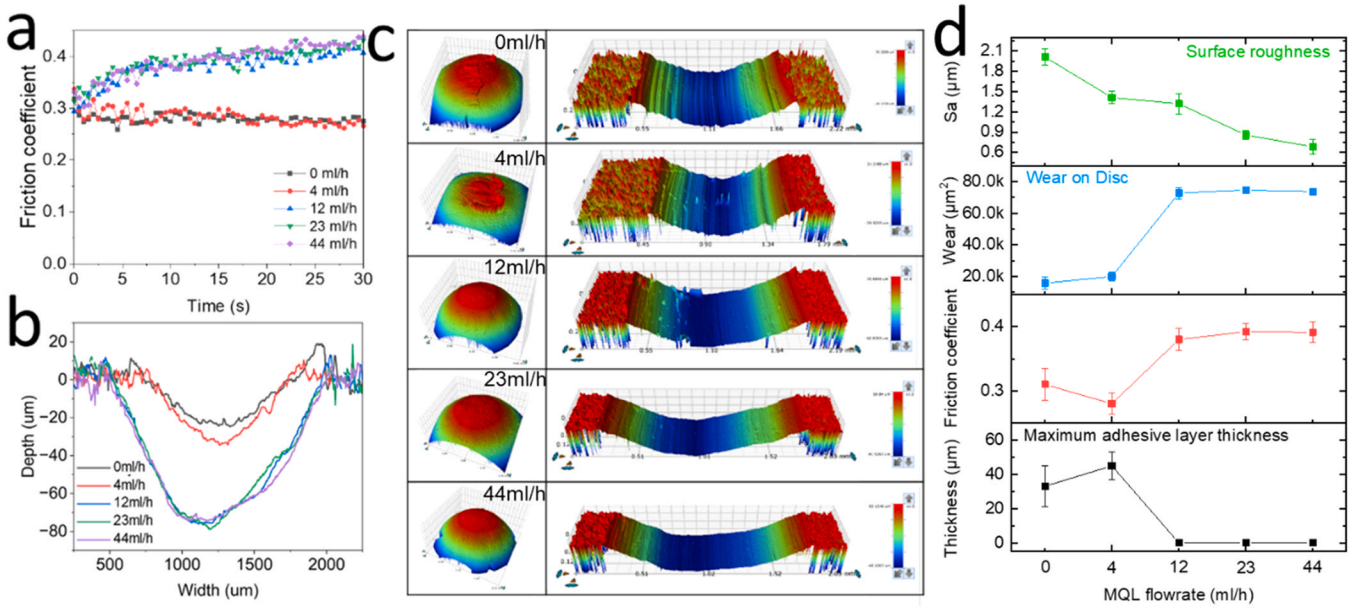

Fig. 6. Effects of oil flow rate on tribological performance and wear characteristics under minimum quantity lubrication (MQL) conditions (WC/Co-Ti64, 30 sec, 47 m/min and 2.5 GPa). (a) Evolution of friction coefficient over time at different oil flow rates (0, 4, 12, 23, and 44 ml/h). (b) Cross-sectional profiles of wear tracks on the disc surface under varying lubrication conditions. (c) 3D surface topographies of wear scars on both pin and disc surfaces corresponding to different oil flow rates. (d) Quantitative comparison of surface roughness of disc wear tracks, wear volume on the disc, average friction coefficient, and maximum adhesive layer thickness as a function of oil flowrate.

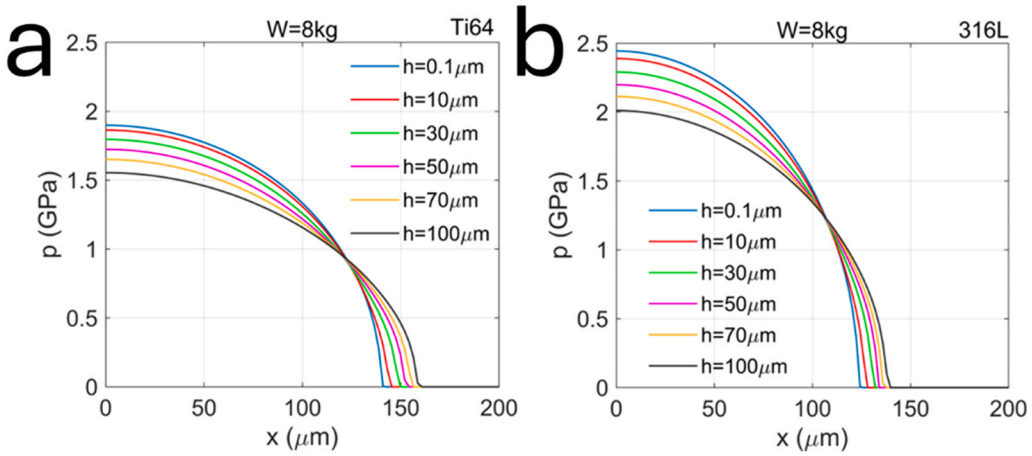

Fig. 7. Contact pressure distribution analysis based on the BEM-based model under a normal load of 8 kg for varying adhesive layer thicknesses. (a) Contact pressure profiles for Ti64 discs with adhesive layer thicknesses ranging from 0.1 μm to 100 μm. (b) Contact pressure profiles for 316 L stainless steel discs under the same conditions. Note: p denotes contact pressure (GPa), and x is contact radius (μm).

Interestingly, although the dry condition is associated with lower nominal contact pressure due to the presence of a Ti64 adhesive layer, it resulted in a thicker work-hardened layer. This finding suggests that adhesive layer formation and the consequent alterations in contact mechanics during dry friction substantially contribute to subsurface strengthening, even when the nominal contact pressure is reduced. This observation also indicates that factors beyond nominal contact pressure, such as stress concentration induced by local surface roughness and irregular wear track morphology, may dominate subsurface deformation.

To further investigate the mechanisms contributing to subsurface deformation and work-hardening behaviour under varying surface and interfacial conditions, BEM-based simulations were conducted to model von Mises stress distributions beneath the disc surface. The roles of surface roughness and the presence of a Ti64 adhesive layer were specifically assessed.

Figs. 9a and 9d show representative surface topographies with roughness (R_q) of 6.9 μm and 0.69 μm, respectively. Under high roughness conditions (R_q = 6.9 μm) and in the absence of an adhesive layer (Fig. 9b), stress concentrations penetrated deeply into the substrate, with normalized von Mises stress reaching approximately 50 at a depth of 20 μm. When a 30 μm Ti64 adhesive layer was introduced (Fig. 9c), the stress intensity at the same depth was decreased to ca. 25, indicating that the adhesive layer partially buffers the transmission of stress into the disc subsurface. At lower surface roughness without adhesive layer (R_q = 0.69 μm, Fig. 9e), the stress was further reduced to ca. 6, with much shallower stress penetration. While the assumed purely elastic contact in these BEM-based simulations may overestimate the magnitude of the nondimensional von Mises stress compared to the practical elastoplastic scenarios, the results functionally support the experimental observations in Fig. 8 and offer a mechanistic explanation for the interesting finding that lower nominal contact pressure in dry

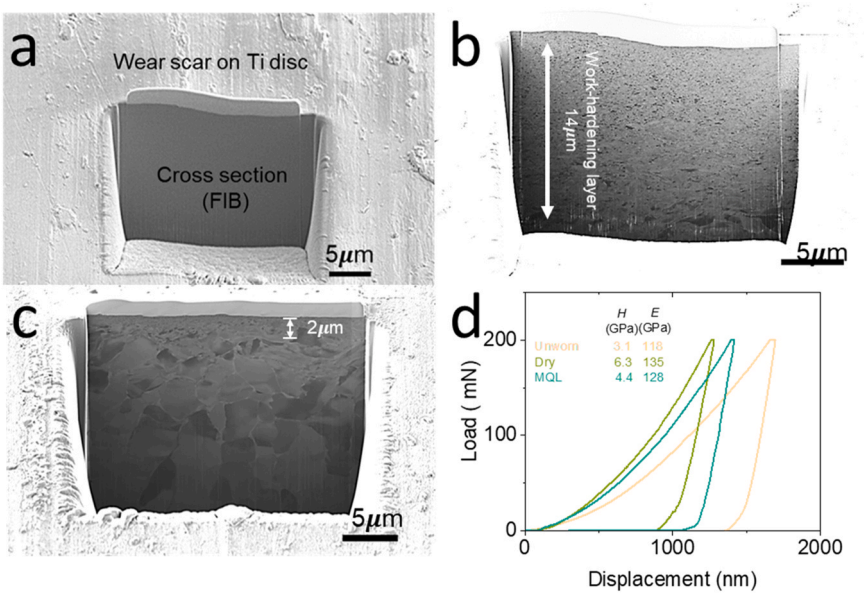

Fig. 8. (a) SEM image showing the cross section on the wear scar of tribo-tested Ti64 disc which is prepared by FIB. (b) SEM images showing the microstructure of top surface on the wear scar of tribo-tested Ti64 disc with different test condition: (a) dry (flowrate of 0 ml/h), 30 sec, 47 m/min and 2.5 GPa; (c) lubricated with MQL (flowrate of 44 ml/h), 30 sec, 47 m/min and 2.5 GPa; (d) Load-displacement response of nano-indentation test on the Ti64 discs. (Unworn: without tribo-test; dry: flowrate of 0 ml/h, 30 sec, 47 m/min and 2.5 GPa; MQL: flowrate of 44 ml/h, 30 sec, 47 m/min and 2.5 GPa).

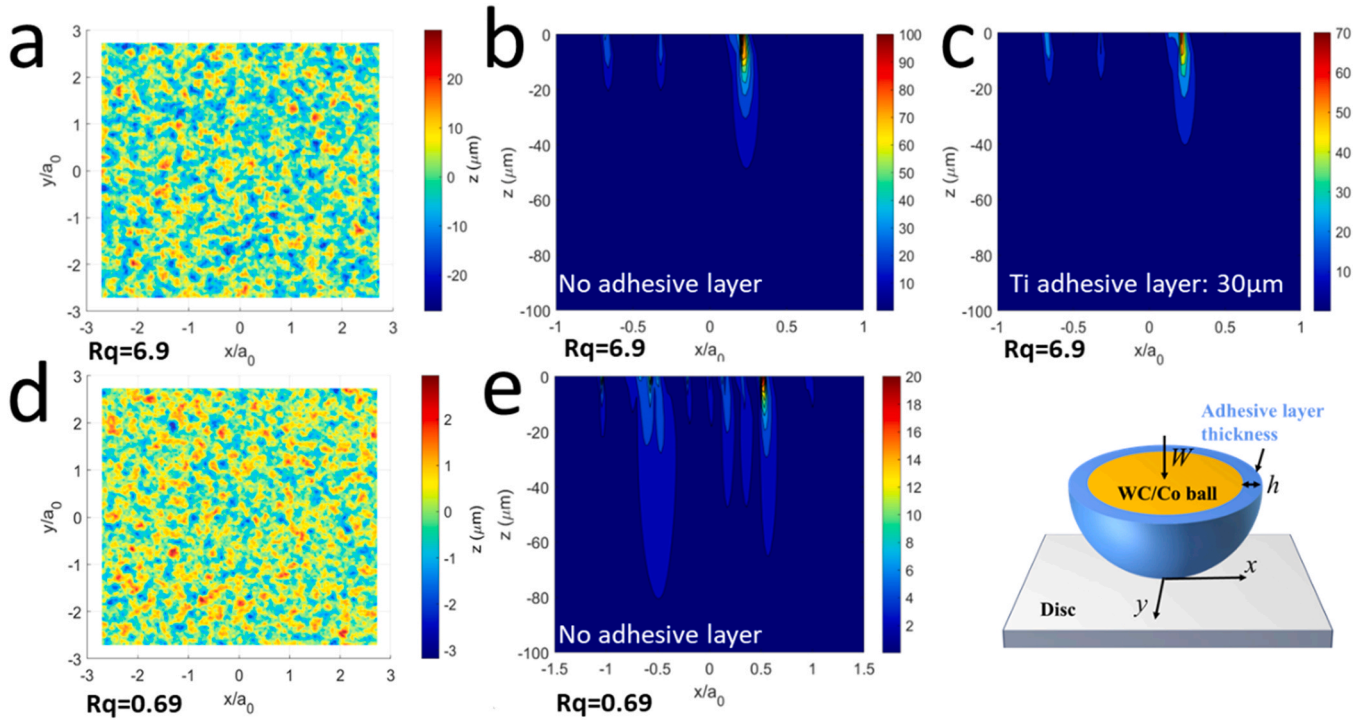

Fig. 9. (a) Surface topography image showing the uniform distribution of asperities on the disc surface with a roughness (R_q) of 6.9 μm. (b) Cross-sectional von Mises stress distribution on the disc surface derived from BEM-based contact analysis (R_q = 6.9 μm, applied load = 18 kg, no adhesive Ti64 layer present on the counterpart pin surface). (c) Cross-sectional von Mises stress distribution on the disc surface derived from BEM-based contact analysis (R_q = 6.9 μm, applied load = 18 kg, adhesive Ti64 layer with a thickness of 30 μm formed on the counterpart pin surface). (d) Surface topography image showing the uniform distribution of asperities on the disc surface with R_q = 0.69 μm. (e) Cross-sectional von Mises stress distribution on the disc surface derived from BEM-based contact analysis (R_q = 0.69 μm, applied load = 18 kg, no adhesive Ti64 layer present on the counterpart pin surface). Note: the unit of the colour bars in (b), (d) and (e) are dimensionless, representing the von Mises stress (σ_{vm}) normalized by the yield stress (σ_{yield}) of Ti64.

sliding conditions can still produce thicker work-hardening layers. This is attributed to the combined effects of local stress concentration from surface asperities and altered interfacial stress distribution caused by the adhesive layer. Compared with the role of adhesive layer in reducing nominal contact pressure, surface roughness has a more dominant influence on local stress concentration, and consequently, on subsurface microstructural deformations.

It should be noted that a significant increase in adhesive layer

thickness on the pin surface can notably influence the wear surface quality of the counterpart disc. A thicker adhesive layer alters the contact geometry during sliding, resulting in increased surface roughness and the development of irregular wear track morphology. This elevated roughness generates localized stress concentrations, which promote the formation of a work-hardening layer beneath the disc surface. The formation of work-hardening layer leads to increased surface brittleness and diminishes the ability of near-surface material to accommodate further plastic deformation, thereby making it more susceptible to crack initiation and propagation during prolonged operation [40,41]. Surface roughness-induced plastic deformation and work-hardening not only dominate the fatigue behavior of machine components but also significantly contribute to other forms of mechanical surface damage [42,43]. These effects are critical in various scenarios, including mechanical damage under repeated bearing pressures without significant lateral sliding, fretting-fatigue characterized by alternating low-amplitude displacements, false brinelling marks in ball or roller bearings, as well as unidirectional friction wear and rolling damage under conditions of both high and low friction, as observed in gears and rolling element bearings [44–47].

4. Conclusion

Both experimental and numerical approaches were employed to systematically investigate the tribological performance and subsurface mechanical responses of Ti64 discs sliding against WC/Co pins. The key findings are:

- Experimentally, Ti64 readily forms thick, intact, and mechanically stable adhesive layers under dry and low MQL flowrate conditions, which corresponds to lower friction coefficients and reduced wear observed on the pin side. However, the presence of these adhesive layers was also associated with increased surface roughness and irregular wear morphology, leading to pronounced local stress concentrations and the development of thicker subsurface work-hardening layers on the Ti64 disc.
- BEM-based simulations confirmed that the adhesive layers reduce nominal contact pressures and subsurface von Mises stresses, contributing to mechanical stabilization at the interface. Nevertheless, the reduced nominal pressure under dry conditions did not suppress subsurface plastic deformation. Instead, elevated local stress concentrations arising from rough surface topography and modified contact geometry were the dominant factors driving subsurface work hardening.
- Cross-sectional analysis and nano-indentation measurements showed that dry sliding conditions significantly increased hardness near the surface compared to high MQL flowrate conditions which produced thinner deformation zones and lower subsurface hardening.
- The comparison with 316 L, included as a reference alloy, helped highlight the distinct tribological behavior of Ti64 and reinforced the material-dependent nature of adhesive layer formation and wear.
- This work presents the first direct evidence of the dual role of adhesive layers: while beneficial for reducing friction and tool-side wear, they can simultaneously intensify surface damage and subsurface deformation on the Ti64 workpiece.
- Surface roughness emerged as the primary factor governing local stress concentration and material response, outweighing the influence of nominal contact pressure.

Therefore, optimizing tribological performance during Ti64 machining requires a balanced control of lubrication flow and surface conditions to promote manageable adhesive layer formation without compromising surface integrity. This work provides critical mechanistic insights for improving machining strategies, tool design, and lubrication protocols aimed at enhancing tool life and ensuring high-quality machined surfaces when working with Ti alloys.

Statement of Originality

I, the Corresponding Author, declare that this manuscript is original, has not been published before and is not currently being considered for publication elsewhere.

I can confirm that the manuscript has been read and approved by all named authors and that there are no other persons who satisfied the criteria for authorship but are not listed. I further confirm that the order of authors listed in the manuscript has been approved by all of us.

I understand that the Corresponding Author is the sole contact for the Editorial process and is responsible for communicating with the other authors about progress, submissions of revisions and final approval of proofs

CRediT authorship contribution statement

Greg de Boer: Writing – review & editing. **Jack Secker:** Writing – review & editing. **Chris Taylor:** Writing – review & editing, Project administration. **Dongze Wang:** Writing – review & editing, Writing – original draft, Methodology, Investigation. **Nan Xu:** Writing – review & editing, Writing – original draft, Methodology, Investigation, Funding acquisition, Conceptualization. **Ardian Morina:** Writing – review & editing, Writing – original draft, Supervision, Project administration, Funding acquisition. **Nikil Kapur:** Writing – review & editing, Supervision, Project administration, Funding acquisition. **Harvey Thompson:** Writing – review & editing.

Declaration of Competing Interest

The authors declare that they have no known competing financial interests or personal relationships that could have appeared to influence the work reported in this paper.

Acknowledgements

The authors gratefully acknowledge the support provided by Mr. Stuart Micklethwaite from the University of Leeds Electron Microscopy and Spectroscopy Centre (LEMAS) for the assistance with the FIB and SEM analyses, and Dr. Chun Wang from the University of Leeds School of Mechanical Engineering for the support with the nanoindentation tests. This research was funded by the Engineering and Physical Sciences Research Council (EPSRC) (Project number: EP/W001950/1, EP/T024542/1) and the Taiho Kogyo Tribology Research Foundation (Project number: 24A27).

Appendix A. Supporting information

Supplementary data associated with this article can be found in the online version at doi:10.1016/j.triboint.2025.111228.

Data availability

Data will be made available on request.

References

[1] Liu S, Shin YC. Additive manufacturing of Ti6Al4V alloy: a review. Mater Des 2019; 164:107552. https://doi.org/10.1016/j.matdes.2018.107552.
[2] Philip JT, Mathew J, Kuriachen B. Tribology of Ti6Al4V: a review. Friction 2019;7: 497–536. https://doi.org/10.1007/s40544-019-0338-7.
[3] Verified Market Reports. Ti-6Al-4V titanium alloy market size, research. Consumer Trends, Analysis & Forecast By 2030. Verified Market Reports; 2024.
[4] Bermingham MJ, Kirsch J, Sun S, Palanisamy S, Dargusch MS. New observations on tool life, cutting forces and chip morphology in cryogenic machining Ti-6Al-4V. Int J Mach Tools Manuf 2011;51:500–11. https://doi.org/10.1016/j.ijmachtools.2011.02.009.

[5] Proud L, Roberts P, Xu N, Wika KK, Morina A, Taylor CM. The tool wear and productivity impact of CO2 and emulsion-based cooling when milling diverse titanium alloys. Wear 2025:206031. https://doi.org/10.1016/j.wear.2025.206031.
[6] Bansal DG, Eryilmaz OL, Blau PJ. Surface engineering to improve the durability and lubricity of Ti–6Al–4V alloy. Wear 2011;271:2006–15. https://doi.org/10.1016/j.wear.2010.11.021.
[7] Li M, Zhao W, Li L, He N, Jamil M. Chatter suppression during milling of Ti-6Al-4V based on variable pitch tool and process damping effect. Machines 2022;10:222. https://doi.org/10.3390/machines10040222.
[8] Khan MA, Imran Jaffery SH, Khan M, Alruqi M. Machinability analysis of Ti-6Al-4V under cryogenic condition. J Mater Res Technol 2023;25:2204–26. https://doi.org/10.1016/j.jmrt.2023.06.022.
[9] Abdelnasser E, Barakat A, Elsanabary S, Nassef A, Elkaseer A. Precision hard turning of Ti6Al4V using polycrystalline diamond inserts: surface quality, cutting temperature and productivity in conventional and High-Speed machining. Materials 2020;13:5677. https://doi.org/10.3390/ma13245677.
[10] Vagnorius Z, Rausand M, Sørby K. Determining optimal replacement time for metal cutting tools. Eur J Oper Res 2010;206:407–16. https://doi.org/10.1016/j.ejor.2010.03.023.
[11] Liang X, Liu Z. Experimental investigations on effects of tool flank wear on surface integrity during orthogonal dry cutting of Ti-6Al-4V. Int J Adv Manuf Technol 2017;93:1617–26. https://doi.org/10.1007/s00170-017-0654-x.
[12] Özel T, Karpat Y. Predictive modeling of surface roughness and tool wear in hard turning using regression and neural networks. Int J Mach Tools Manuf 2005;45:467–79. https://doi.org/10.1016/j.ijmachtools.2004.09.007.
[13] Ulutan D, Ozel T. Machining induced surface integrity in titanium and nickel alloys: a review. Int J Mach Tools Manuf 2011;51:250–80. https://doi.org/10.1016/j.ijmachtools.2010.11.003.
[14] Sartori S, Moro L, Ghiotti A, Bruschi S. On the tool wear mechanisms in dry and cryogenic turning additive manufactured titanium alloys. Tribology Int 2017;105:264–73. https://doi.org/10.1016/j.triboint.2016.09.034.
[15] Liu H, Ayed Y, Birembaux H, Rossi F, Poulachon G. Impacts of flank wear and cooling strategies on evolutions of built-up edges, diffusion wear and cutting forces in Ti6Al4V machining. Tribology Int 2022;171:107537. https://doi.org/10.1016/j.triboint.2022.107537.
[16] Liang X, Liu Z, Wang B, Song Q, Cai Y, Wan Y. Prediction of residual stress with multi-physics model for orthogonal cutting Ti-6Al-4V under various tool wear morphologies. J Mater Process Technol 2021;288:116908. https://doi.org/10.1016/j.jmatprotec.2020.116908.
[17] Lin S, Peng F, Wen J, Liu Y, Yan R. An investigation of workpiece temperature variation in end milling considering flank rubbing effect. Int J Mach Tools Manuf 2013;73:71–86. https://doi.org/10.1016/j.ijmachtools.2013.05.010.
[18] Karpat Y, Özel T. Predictive analytical and thermal modeling of orthogonal cutting Process—Part II: effect of tool flank wear on tool forces, stresses, and temperature distributions. J Manuf Sci Eng 2006;128:445–53. https://doi.org/10.1115/1.2162591.
[19] Toubhans B, Fromentin G, Viprey F, Karaouni H, Dorlin T. Machinability of inconel 718 during turning: cutting force model considering tool wear, influence on surface integrity. J Mater Process Technol 2020;285:116809. https://doi.org/10.1016/j.jmatprotec.2020.116809.
[20] Bleicher F, Pollak C, Brier J, Siller A. Reduction of built-up edge formation in machining Al- and cast iron hybrid components by internal cooling of cutting inserts. CIRP Ann 2016;65:91–100. https://doi.org/10.1016/j.cirp.2016.04.090.
[21] Wang Z, Kovvuri V, Araujo A, Bacci M, Hung WNP, Bukkapatnam STS. Built-up-edge effects on surface deterioration in micromilling processes. J Manuf Process 2016;24:321–7. https://doi.org/10.1016/j.jmapro.2016.03.016.
[22] Oliaei SNB, Karpat Y. Built-up edge effects on process outputs of titanium alloy micro milling. Precis Eng 2017;49:305–15. https://doi.org/10.1016/j.precisioneng.2017.02.019.
[23] Oliaei SNB, Karpat Y. Investigating the influence of built-up edge on forces and surface roughness in micro scale orthogonal machining of titanium alloy Ti6Al4V. J Mater Process Technol 2016;235:28–40. https://doi.org/10.1016/j.jmatprotec.2016.04.010.
[24] Chowdhury MSI, Chowdhury S, Yamamoto K, Beake BD, Bose B, Elfizy A, Cavelli D, Dosbaeva G, Aramesh M, Fox-Rabinovich GS, Veldhuis SC. Wear behaviour of coated carbide tools during machining of Ti6Al4V aerospace alloy associated with strong built up edge formation. Surf Coat Technol 2017;313:319–27.
[25] Saketi S, Odelros S, Östby J, Olsson M. Experimental study of wear mechanisms of cemented carbide in the turning of Ti6Al4V. Materials 2019;12:2822. https://doi.org/10.3390/ma12172822.
[26] Sharma S, Meena A. Microstructure attributes and tool wear mechanisms during high-speed machining of Ti-6Al-4V. J Manuf Process 2020;50:345–65. https://doi.org/10.1016/j.jmapro.2019.12.029.
[27] Younas M, Khan M, Jaffery SHI, Khan Z, Khan N. Investigation of tool wear and energy consumption in machining Ti6Al4V alloy with uncoated tools. Int J Adv Manuf Technol 2024;132:3785–99. https://doi.org/10.1007/s00170-024-13548-1.
[28] Zhang P, Li SX, Zhang ZF. General relationship between strength and hardness. Materials Science Engineering A 2011;529:62–73. https://doi.org/10.1016/j.msea.2011.08.061.
[29] Pavlina EJ, Van Tyne CJ. Correlation of yield strength and tensile strength with hardness for steels. J Mater Eng Perform 2008;17:888–93. https://doi.org/10.1007/s11665-008-9225-5.
[30] Boussinesq J. Applications des potentiels à l'étude de l'équilibre et mouvement des solides elastiques. GauthierVilla Paris 1885.
[31] Cerruti V. Ricerche intorno all' equilibrio de'corpi elastici isotropi. Atti R Accad Lince Mem Cl Sci Fis Mat e Nat 1882;3:81–122.
[32] Wang D, Ghanbarzadeh A, Xu N, Liu Q, De Boer G. Time-Dependent contact behaviour of ZDDP-Derived tribofilms: a viscoelastic layered model approach. Tribol Lett 2025;73:69. https://doi.org/10.1007/s11249-025-01990-5.
[33] Liu S, Wang Q. Studying contact stress fields caused by surface tractions with a discrete convolution and fast Fourier transform algorithm. J Tribology 2002;124:36–45. https://doi.org/10.1115/1.1401017.
[34] Polonsky IA, Keer LM. A numerical method for solving rough contact problems based on the multi-level multi-summation and conjugate gradient techniques. Wear 1999;231:206–19. https://doi.org/10.1016/S0043-1648(99)00113-1.
[35] Wang Z-J, Wang W-Z, Wang H, Zhu D, Hu Y-Z. Partial slip contact analysis on Three-Dimensional elastic layered half space. J Tribology 2010;132:021403. https://doi.org/10.1115/1.4001011.
[36] Archard JF. The temperature of rubbing surfaces. Wear 1959;2:438–55. https://doi.org/10.1016/0043-1648(59)90159-0.
[37] Akchurin A, Bosman R, Lugt PM. A Stress-Criterion-Based model for the prediction of the size of wear particles in boundary lubricated contacts. Tribol Lett 2016;64:35. https://doi.org/10.1007/s11249-016-0772-x.
[38] Li T, Shi J, Wang S, Zio E, Ma Z. Mesoscale numerical modeling for predicting wear debris generation. Tribol Lett 2019;67:38. https://doi.org/10.1007/s11249-019-1150-2.
[39] Hukkerikar AV, Arrazola P-J, Aristimuño P, Norgren S, Morandeau A, Joly D. A tribological characterisation of Ti-48Al-2Cr-2Nb and Ti-6Al-4V alloys with dry, flood, and MQL lubricants. CIRP J Manuf Sci Technol 2023;41:501–23. https://doi.org/10.1016/j.cirpj.2022.11.016.
[40] Farokhzadeh K, Edrisy A. Transition between mild and severe wear in titanium alloys. Tribology Int 2016;94:98–111. https://doi.org/10.1016/j.triboint.2015.08.020.
[41] Tobi ALM, Sun W, Shipway PH. Evolution of plasticity-based wear damage in gross sliding fretting of a Ti-6Al-4V non-conforming contact. Tribology Int 2017;113:474–86. https://doi.org/10.1016/j.triboint.2017.01.010.
[42] Schubnell J, Pontner P, Wimpory RC, Farajian M, Schulze V. The influence of work hardening and residual stresses on the fatigue behavior of high frequency mechanical impact treated surface layers. Int J Fatigue 2020;134:105450. https://doi.org/10.1016/j.ijfatigue.2019.105450.
[43] Tiwari A, Almqvist A, Persson BNJ. Plastic deformation of rough metallic surfaces. Tribol Lett 2020;68:129. https://doi.org/10.1007/s11249-020-01368-9.
[44] Barrois W. Repeated plastic deformation as a cause of mechanical surface damage in fatigue, wear, fretting-fatigue, and rolling fatiguea review. Int J Fatigue 1979;1:167–89. https://doi.org/10.1016/0142-1123(79)90022-7.
[45] Wang D, Zhang D, Ge S. Effect of displacement amplitude on fretting fatigue behavior of hoisting rope wires in low cycle fatigue. Tribology Int 2012;52:178–89. https://doi.org/10.1016/j.triboint.2012.04.008.
[46] Zambrano OA, Gómez JA, Coronado JJ, Rodríguez SA. The sliding wear behaviour of steels with the same hardness. 418–419:201–7 Wear 2019. https://doi.org/10.1016/j.wear.2018.12.002.
[47] Ueda M, Wainwright B, Spikes H, Kadiric A. The effect of friction on micropitting. Wear 2022;488–489:204130. https://doi.org/10.1016/j.wear.2021.204130.